photonics

MDPI

Article

Enhancing the Overall Performance of Perovskite Solar Cells with a Nano-Pyramid Anti-Reflective Layer

Li Liu [1,*], Wenfeng Liu [2], Wenfeng Fu [1], Zao Yi [1,3,*], Yougen Yi [2], Jianguo Zhang [4], Chaojun Tang [5], Tangyou Sun [6], Qingdong Zeng [7] and Pinghui Wu [8]

1 Joint Laboratory for Extreme Conditions Matter Properties, Key Laboratory of Manufacturing Process Testing Technology of Ministry of Education, State Key Laboratory of Environment-Friendly Energy Materials, Southwest University of Science and Technology, Mianyang 621010, China; fuwenfeng2021@163.com
2 School of Energy Science and Engineering, College of Physics, Central South University, Changsha 410083, China; 193902015@csu.edu.cn (W.L.); yougenyi@csu.edu.cn (Y.Y.)
3 School of Chemistry and Chemical Engineering, Jishou University, Jishou 416000, China
4 Department of Physics, Jinzhong University, Jinzhong 030619, China; phys.zhangjg@gmail.com
5 College of Science, Zhejiang University of Technology, Hangzhou 310023, China; chaojuntang@126.com
6 Guangxi Key Laboratory of Precision Navigation Technology and Application, Guilin University of Electronic Technology, Guilin 541004, China; suntangyou@guet.edu.cn
7 School of Physics and Electronic-information Engineering, Hubei Engineering University, Xiaogan 432000, China; zengqingdong2005@163.com
8 Office of Science and Technology, Quanzhou Normal University, Quanzhou 362000, China; phwu@zju.edu.cn
* Correspondence: liuli_phy@swust.edu.cn (L.L.); yizaomy@swust.edu.cn (Z.Y.); Tel.: +86-0816-2480830 (Z.Y.); Fax: +86-0816-2480830 (Z.Y.)

Abstract: Perovskite solar cells (PSCs) still suffer from varying degrees of optical and electrical losses. To enhance the light decoupling and capture ability of Planar PSCs, an ultra-thin PSC structure with an Al_2O_3 pyramid anti-reflection layer (Al_2O_3 PARL) is proposed. The effect of the structure of the Al_2O_3 PARL on the photoelectric performance of PSCs was investigated by changing various parameters. Under the AM1.5 solar spectrum (300–800 nm), the average light absorption rates and quantum efficiency (QE) of PSCs containing pyramid-array textured rear layers (PARLs) were significantly higher than those of planar PSCs. The Al_2O_3 PARL-based PSCs achieved a light absorption rate of 96.05%. Additionally, electrical simulations were performed using the finite element method (FEM) to calculate the short-circuit current density (J_{SC}), open-circuit voltage (V_{OC}), and maximum power (Pmax). Based on the maximum value of the average light absorbance, the geometric structure of the Al_2O_3 pyramid PSCs was optimized, and the optimization results coincided with the J_{SC} and QE results. The results of the electrical simulation indicated that the maximum J_{SC} was 23.54 mA/cm^2. Additionally, the J_{SC} of the Al_2O_3 pyramid PSCs was 22.73% higher than that of planar PSCs, resulting in a photoelectric conversion efficiency (PCE) of 24.34%. As a result, the photoelectric conversion rate of the solar cells increased from 14.01% to 17.19%. These findings suggest that the presence of the Al_2O_3 PARL enhanced photon absorption, leading to an increase in electron–hole pairs and ultimately improving the photocurrent of the solar cells.

Keywords: perovskite solar cells; pyramid structure; photoelectric conversion efficiency; solar energy absorption

check for updates

Citation: Liu, L.; Liu, W.; Fu, W.; Yi, Z.; Yi, Y.; Zhang, J.; Tang, C.; Sun, T.; Zeng, Q.; Wu, P. Enhancing the Overall Performance of Perovskite Solar Cells with a Nano-Pyramid Anti-Reflective Layer. *Photonics* **2024**, *11*, 715. https://doi.org/10.3390/photonics11080715

Received: 30 May 2024
Revised: 27 July 2024
Accepted: 28 July 2024
Published: 31 July 2024

Copyright: © 2024 by the authors. Licensee MDPI, Basel, Switzerland. This article is an open access article distributed under the terms and conditions of the Creative Commons Attribution (CC BY) license (https://creativecommons.org/licenses/by/4.0/).

1. Introduction

Perovskite materials are different from other common semiconductor materials; they have stronger optoelectronic performance, with advantages including a high light absorption coefficient, adjustable diffusion length, low processing cost, and so on, attracting a lot of photovoltaic field scholars' and industrial researchers' attention [1–6]. However, when sunlight enters from one medium into another medium, according to the Fresnel reflection principle, a reflection occurs at the interface between the two media, and the greater the

difference in refractive index between the two media, the stronger the reflection will be. We know that there is a certain degree of optical loss in the existing perovskite solar cells (PSCs), and the light absorption efficiency is low, seriously restricting the energy efficiency improvement [7,8]. At the same time, due to the high optical loss, the perovskite light absorption layer cannot absorb enough photons, thus cannot generate enough electron–hole pairs, limiting the electrical performance. In existing research [9,10], many scholars have added a high-performance anti-reflection film to the transparent substrate of PSCs. The presence of the anti-reflection film enables solar cells to achieve broadband absorption, thus effectively improving the PCE. It also effectively isolates solar cells from the external environment, reducing the impact of wind and rain on solar cells and minimizing losses [11]. Al_2O_3 material has a refractive index of about 1.62 in the visible light region, and it is often used with MgF_2 and ZrO_2 to coat the visible light region of the anti-reflection film. Generally, physical vapor deposition (PECVD) or solution-based methods are used to prepare Al_2O_3 thin films, ensuring the selection of high-purity precursor materials [12,13]. During PECVD, deposition temperature, gas flow rates, and deposition time were controlled to achieve obtain uniform and dense Al_2O_3 films. These methods can control the thickness and morphology of the film to achieve optimal antireflection effects. Traditional materials such as TiO_2 and SnO_2 exhibit good transparency in the visible light range, but their electron transport properties are relatively poor. This can lead to recombination of electron–hole pairs, thereby reducing solar cell efficiency. Additionally, some traditional materials are sensitive to humidity and oxygen, which can lead to degradation and impact solar cells' lifespan. In summary, the Al_2O_3 pyramid structure holds potential as a novel antireflection coating material for solar cells, but further research and optimization are still needed. Al_2O_3 has excellent corrosion resistance, wear resistance, and heat resistance, with both very high surface stability and excellent adhesion, and it can be closely combined with glass substrate, giving it excellent optical performance, making it an ideal anti-reflection film material. In addition, texturing the Al_2O_3 anti-reflection film can further enhance light capture efficiency, thereby improving light absorption. Texturing can involve a variety of different nanostructures, including but not limited to nanowires [14,15], nanorods [16,17], nanocones [18,19], nanoholes [19,20], and so on. Compared with the above nanostructures, nanopyramids have smaller surface recombination, more suitable for solar cells. The nanopyramid Al_2O_3 anti-reflection film significantly enhances light absorption in the solar cell, thereby boosting energy conversion efficiency [21–23]. Incident light interacting with different positions of the Al_2O_3 pyramid structure experiences varying refractive indices, known as the refractive index gradient effect. This effect enhances light capture efficiency and accentuates the cone profile [24]. The side walls of the Al_2O_3 pyramid structure create multiple light-scattering effects, increasing the path length of photons within the active layer, which enhances light capture. Based on this understanding of the anti-reflection performance of the Al_2O_3 pyramid structure, we integrated this structure into planar PSCs to reduce optical losses and enhance light capture capability [25].

This paper proposes PSCs based on an Al_2O_3 pyramid anti-reflection layer structure (Al_2O_3 PARLs). The change of the optoelectronic performance of the designed cells under different geometric parameters of Al_2O_3 PARLs was studied. When the Al_2O_3 pyramid height h = 200 nm, bottom length d = 200 nm, the performance of the solar cell was the best, and its PCE increased to 17.19%. Comparing these structural parameters with the planar PSCs, the comparison results revealed that the Al_2O_3 pyramid PSCs on the surface had an average light absorption of 96.05%, much higher than the planar PSCs. Al_2O_3 PARLs had the effect of reducing the reflectivity, improving the PSCs' light absorption and quantum efficiency (QE). According to the calculated electric field intensity distribution map, the Al_2O_3 pyramid structure had a strong light coupling effect, corresponding to its light absorption results. Through electrical simulation, the maximum short-circuit current density of this Al_2O_3 pyramid PSCs was found to be 23.54 mA/cm^2, increasing by 4.36 mA/cm^2compared with the planar PSCs' short-circuit current density of 19.18 mA/cm^2, and the PCE increased from 14.01% to 17.19%. The calculation results will be useful for developing and manufac-

turing the next generation of high-efficiency solar cells, providing detailed guidance for PSCs with energy conversion efficiency.

2. Model Structure

Figure 1a shows the high-efficiency planar single-junction PSCs we designed. The structure from top to bottom was a 200 nm thick FTO/glass substrate, a 150 nm thick TiO_2 electron transport layer (ETL), and a 500 nm $CH_3NH_3PbI_3$ perovskite active layer, placed on a 250 nm Spiro-OMeTAD hole transport layer (HTL). Finally, 100 nm thick Au was used as the electrode to complete this planar single-junction PSC. All geometric parameters were optimized based on FDTD software (FDTD 8.15.736) [26–28]. Figure 1b illustrates the energy band diagram of carrier transport in the designed PSC, wherein the contact between each layer exhibits a gradient increasing band gap. This configuration ensured favorable valence band matching, provided a nearly constant V_{OC}, and enhanced the FF by facilitating carrier transport and reducing the loss of carrier complexes in the absorber layer. The planar PSC design shown in Figure 1a does not allow enough photons to be absorbed in the active $CH_3NH_3PbI_3$ layer, resulting in corresponding reflection losses. To enhance the light decoupling and light capture capabilities of these planar PSCs, this paper proposes PSCs with an Al_2O_3 PARL structure based on the designed planar PSCs, as shown in Figure 1c. Figure 1d shows a section of the designed model. In this design, the PSC surface is textured with an Al_2O_3 pyramid anti-reflection film with a length-to-width ratio of 1(d = w) and a height of h, as shown in Figure 1e, using additional means to optimize light decoupling and light capture, providing an effective structure for optimizing photon management of single-junction PSCs. Since the metal oxide Al_2O_3 has a refractive index comparable with perovskite materials, when the incident light propagates from the air medium to the solar cell, this Al_2O_3 pyramid can serve as a refractive index gradient. The incident light produces different refractive indices at different positions of the Al_2O_3 pyramid structure. When the equivalent refractive index curve of the Al_2O_3 pyramid gradually increases from top to bottom, the gradient change of the refractive index with the surrounding air gradually decreases, thereby reducing the reflectance of the incident light. Using this gradient refractive index characteristic of the Al_2O_3 pyramid, we can reduce the reflectance of the PSCs in the wide band from 300 nm to 800 nm, thereby improving the light absorption efficiency. In the optical simulation stage, we used the finite-difference time-domain method (FDTD) to study the optical properties of the planar PSCs and the PSCs with the Al_2O_3 PARL structure. Due to its high accuracy and wideband frequency coverage, Lumerical FDTD is one of the most suitable commercial software tools for detecting the optical performance of optoelectronic devices [29,30]. The complex refractive index of the material obtained from the experiment was used as the optical simulation parameter input to the FDTD material library [31,32]. In FDTD, we set the wavelength range to between 300 nm and 800 nm, and the plane wave incident perpendicular to the PSCs surface. The wave source was placed in the air, and periodic boundary conditions were set in the *X*-axis and *Y*-axis directions, so that periodicity was established in the entire designed PSC structure. To avoid parasitic emission and absorption of electromagnetic waves, we set the boundary conditions along the *Z*-axis direction to be a perfect matching layer (PML). In all simulation cases, the grid size was 5 nm. Through FDTD optical simulation, the generated electron–hole pairs were used as optical inputs for finite element simulation, and then, the photo-generated carrier rate was simulated via finite element method (FEM) technology for electrical simulation [33,34]. For the electrical simulation, we calculated the electronic parameters of the materials used from the literature [35,36].

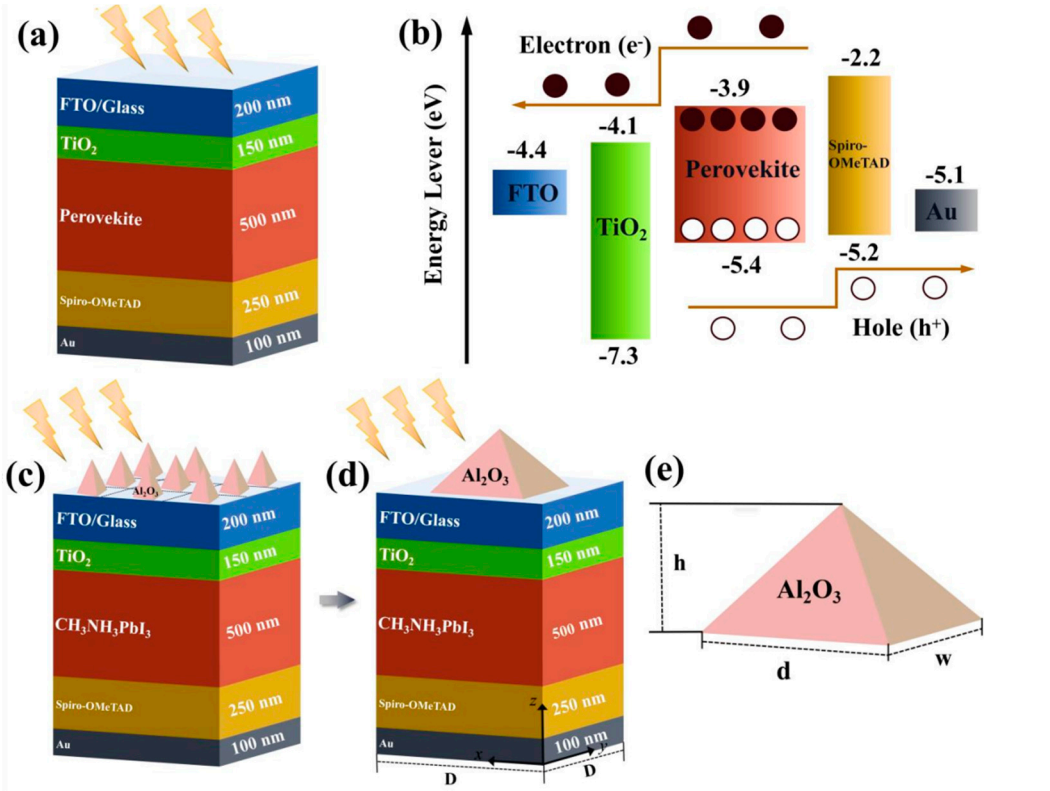


Figure 1. (**a**) Diagram of planar PSCs; (**b**) energy band diagram of carrier transport in the designed PSCs; (**c**) diagram of Al_2O_3 pyramid PSCs; (**d**) part of the structure; (**e**) the dimensional details of one pyramid of the Al_2O_3 PARL (d:w = 1:1).

In the FDTD simulation phase, we used plane waves with wavelengths between 300 nm and 800 nm incident on the solar cell surface in the negative *Z* direction. We used periodic boundary conditions in the *X* and *Y* directions [37–39]. To eliminate parasitic reflections and absorption of electromagnetic waves in the *Z* direction, we used perfectly suited layer (PML) boundary conditions [40,41]. FDTD can calculate the optical power that is absorbed on a per unit volume basis [42], which is defined by the following formula [43]:

$$\mathrm{Pabs} = -0.5\omega|\mathrm{E}|^2\mathrm{Im}\{\varepsilon\} \tag{1}$$

where E is the electric field in the type, the angular frequency of the electromagnetic wave is the dielectric constant, and $\mathrm{Im}\{\varepsilon\}$ is the imaginary part of the dielectric constant. Under the AM1.5 solar spectrum, which was used to determine an important parameter of the solar cells, namely J_{SC}, the ideal J_{SC} value can be calculated by the following formula under the assumption that every photon absorbed by the active layer generates an electron–hole pair [44]:

$$J_{sc} = \frac{q}{2\pi\hbar c}\int_{300nm}^{800nm} \lambda Q_E(\lambda) I_{AM1.5} \lambda d_\lambda \tag{2}$$

where Q is the charge of the electron, λ is the wavelength of the light source, C is the speed of light in a vacuum, $Q_E(\lambda)$ is the QE of the solar cells in the formula, and $I_{AM1.5}$ represents the solar irradiance under AM1.5. The following formula expresses the amount of photogenerated carriers per unit volume [45]:

$$G = \frac{\mathrm{Pabs}}{2\Pi\hbar\omega} = -\frac{0.5\mathrm{Im}\{\varepsilon\}}{\hbar} \tag{3}$$

where $\hbar$ is the reduced Planck's constant and $2\pi\omega$ is the corresponding frequency of photon energy. G, the total number of photogenerated carriers [46], is integrated over the

entire range and depends on frequency and space. According to the relevant physical theory expressed in the formula, we calculated the photogenerated charge carriers using the FDTD software (FDTD 8.15.736) which were then imported into the Comsol software (Comsol 6.1.0.357) for the electrical simulations. With the support of this theory, we obtained the J_{SC}, V_{OC}, Pmax, and other electrical parameters of the solar cells.

In order to measure the actual photovoltaic performance of the solar cells, electrical simulation of the designed solar cells was carried out using the finite element method to determine the various electrical parameters of the calcium titanite solar cells, such as J_{SC}, V_{OC}, fill factor, and photovoltaic conversion efficiency. In the finite element method, a geometrical model of the designed solar cells was first created, the material parameters of the modeling region, boundary conditions, scanning voltages, and mesh size dimensions were defined and finally, the simulation was run. Electrical simulations were performed using the finite element method and the device characteristics were controlled by semiconductor equations, including nonlinear Poisson, continuity, and drift-diffusion equations. Four types of composite mechanisms were also considered in the electrical simulations [47]:

$$R_{rad} = B\left(n_p - n_i^2\right) \tag{4}$$

$$R_{Aug} = \left(nC_n + pC_p\right)\left(n_p - n_i^2\right) \tag{5}$$

$$R_{SRH} = \frac{n_p - n_i^2}{\tau_p(n + n_t) + \tau_n(p + p_t)} \tag{6}$$

$$R_{Surf} = \frac{n_p - n_i^2}{\frac{1}{S_p}(n + n_{ts}) + \frac{1}{S_n}(p + p_s)} \tag{7}$$

where R_{rad} is radiation recombination, R_{Aug} is non-radiative recombination, i.e., Auger recombination, R_{SRH} is Shockley–Read–Hall recombination, and R_{Surf} is surface recombination, B is the radiation recombination coefficient, C_n is the electron Auger recombination coefficient, C_P is the hole Auger recombination coefficient, τn and τp are the lifetimes of electrons and holes, respectively, S_n and S_p are the surface recombination velocities of electrons and holes, respectively, and ni is the intrinsic carrier concentration. Through FDTD optical simulation, the generated electron–hole pairs were used as optical inputs for the finite element simulation, which was able to accurately simulate the electrical performance of the solar cell devices. The generation rates of electrons and holes remained constant at the total generation rate:

$$G_{total} = G_n = G_p \tag{8}$$

In addition, the basic electronic properties of the materials were also used in the calculations. Based on the above formulas, the electrical characteristics of the solar cells were calculated using the finite element technology, and the light absorption curve, QE curve, and various electrical simulation data of the PSCs were obtained.

3. Results and Analysis

The Al_2O_3 PARLs were able to effectively reduce the reflection of solar energy and increase the light transmission rate in the PSCs. According to the gradient refractive index effect, different base and height ratios of the pyramid led to different anti-reflection effects, and the light absorption in the PSCs was different [48]. In order to study the specific optical properties of the PSCs with the Al_2O_3 PARLs, we studied the changes in the optical properties of the PSCs designed with different Al_2O_3 PARLs. First, we fixed the bottom width d = 200 nm of the Al_2O_3 pyramid structure and explored the effect of different heights h on the light absorption rate of the designed PSCs, as shown in Figure 2a. The light absorption curve results showed that in the entire wavelength range we calculated, when the height of the Al_2O_3 pyramid was 100 nm, the light absorption rate of the designed PSCs was the lowest. As the height of the Al_2O_3 pyramid increased, the light absorption

of the PSCs gradually increased and stabilized. The light absorption rates of the Al_2O_3 pyramid at 200 nm, 300 nm, and 400 nm were not much different. This is because when the height of the Al_2O_3 pyramid increased to a certain level, the light absorption of the PSCs reached its limit, and the overly high Al_2O_3 pyramid hindered a small part of the light absorption [49]. Figure 2b explores the average light absorption of the designed PSCs calculated under different Al_2O_3 pyramid structure heights h. In addition, it is apparent in Figure 2b that from 100 nm to 200 nm, as the height of the Al_2O_3 pyramid increased, the average light absorption rate increased from 87.42% to 96.05%, but when the height h of the Al_2O_3 pyramid increased to 300 nm or 400 nm, the average light absorption of the solar cell gradually began to decrease. From Figure 2, we can conclude that when the height h of the Al_2O_3 PARLs was 200 nm, the average light absorption rate of the solar cell was the largest at 96.05%. This shows that as the thickness of the Al_2O_3 pyramid increased, the light absorption of the solar cell increased with the increase in thickness and then gradually decreased.

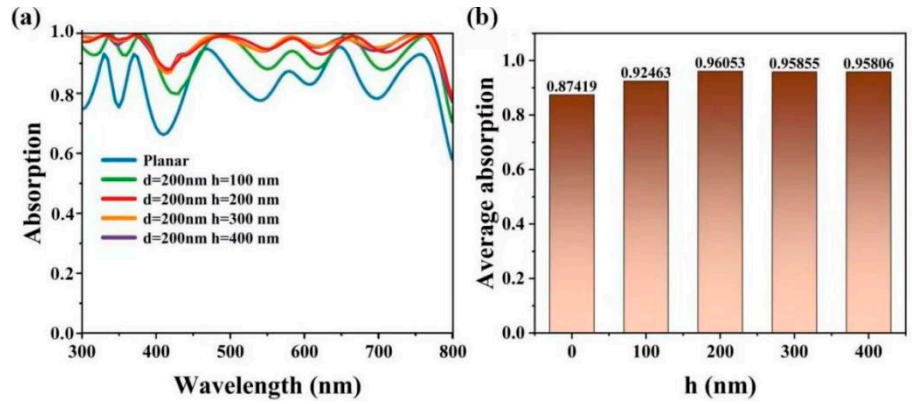


Figure 2. At different heights of the Al_2O_3 pyramid, (**a**) the absorption spectra of the designed cells; (**b**) the average light absorbance of the designed cells.

To further explore the optical performance of Al_2O_3 pyramid PSCs, we also studied the effect of different bottom side lengths of the Al_2O_3 pyramids on the optical performance of the designed PSCs. Figure 3a shows that as the bottom side length d of the Al_2O_3 pyramid increased from 40 nm to 200 nm, the light absorption of the solar cell gradually increased; however, when d increased from 200 nm to 280 nm, the light absorption of the solar cell decreased. Figure 3b shows more clearly that when the bottom side length d of the Al_2O_3 pyramid was 200 nm, the average light absorption of the solar cell was at its highest.

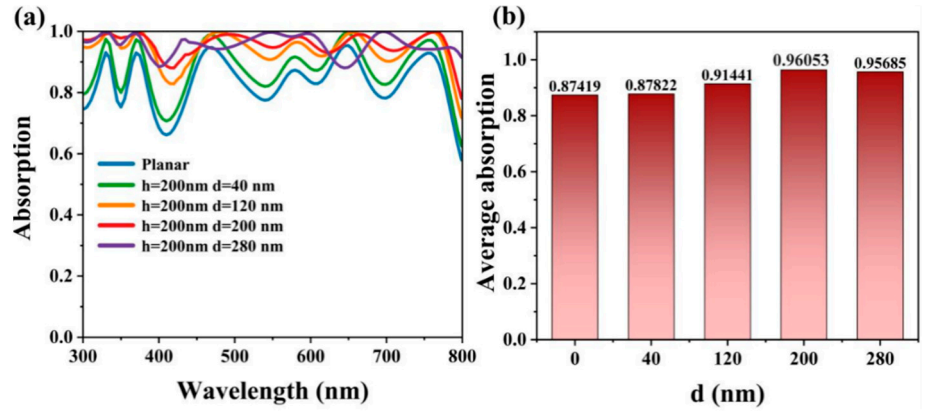


Figure 3. At different bottom side lengths of the Al_2O_3 pyramid, (**a**) the absorption spectra of PSCs; (**b**) the average light absorption rate of the PSCs.

Electrical performance is an important indicator of solar cells [50,51]. In order to better reveal the photoelectric performance of Al_2O_3 pyramid PSCs, we used the finite element

method (FEM) to simulate the electrical performance of cells with different Al_2O_3 PARL parameters. The specific electrical performance parameters of the solar cells at different Al_2O_3 pyramid heights are shown in Table 1, below. These results were consistent with the absorption. As shown in Figure 4a, illustrating the J-V curves, we explored the changes in J_{SC} of the solar cells with different Al_2O_3 pyramid heights. In the figure, 'Planar' represents a perovskite solar cell without Al_2O_3 PARLs. From Figure 4a, it can be clearly seen that the J_{SC} of the PSCs without Al_2O_3 PARLs was the lowest at 19.18 mA/cm^2. When the height of the Al_2O_3 pyramid increased from 100 nm to 200 nm, the J_{SC} increased from 21.48 mA/cm^2 to 23.54 mA/cm^2, because as the height of the Al_2O_3 pyramid increased, the anti-reflection performance of the Al_2O_3 pyramid also increased [52]. When the heights of the Al_2O_3 pyramid were 200 nm, 300 nm, and 400 nm, the J-V curves of the solar cells almost coincided, indicating that as the height of the Al_2O_3 pyramid increases, the J_{SC} of the solar cell no longer increased. The calculation results showed that when the height h of the Al_2O_3 pyramid was 200 nm, the J_{SC} of the designed cell was the largest, J_{SC} = 23.54 mA/cm^2. As shown in Figure 4b, the P-V curves was basically the same as the J-V curves at different Al_2O_3 pyramid heights.

Table 1. Specific Electrical Performance Parameters of Cells with Different Al2O3 Pyramid Heights.

H (nm)	V_{OC} (V)	J_{SC} (mA/cm^2)	PCE (%)
Planar	0.89	19.18	14.01
100	0.89	21.48	15.50
200	0.90	23.54	17.19
300	0.90	23.41	17.06
400	0.90	23.32	16.98

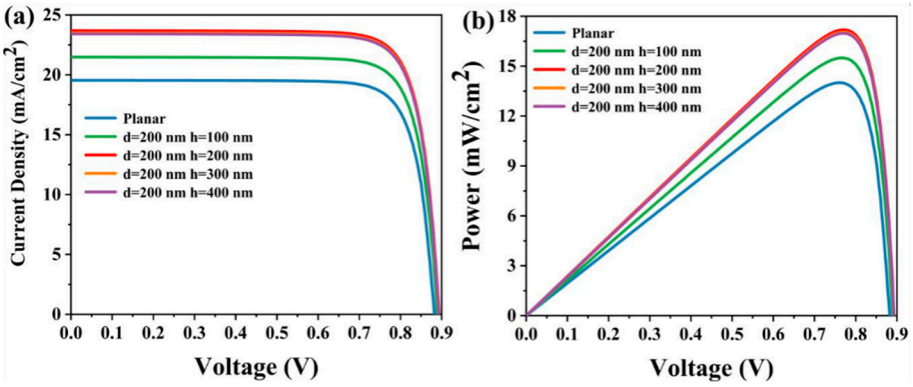


Figure 4. (**a**,**b**) the J-V curves and P-V curves of the designed PSCs with different heights of Al_2O_3 pyramids, respectively (d = w = 200 nm).

Figure 5a,b, respectively, show the J-V curves and P-V curves of the designed PSCs when the bottom side length d of the surface Al_2O_3 pyramid was 40 nm, 120 nm, 200 nm, and 280 nm (the height of the Al_2O_3 pyramid was fixed at 200 nm). The curve results showed that under the Al_2O_3 PARLs, when the bottom side length d = 200 nm, the maximum short-circuit current density was 23.54 mA/cm^2. When d = 40 nm, the minimum short-circuit current density of the solar cell was 20.67 mA/cm^2. The corresponding P-V curves and J-V curves showed that when d = 200 nm, the maximum electrical power of the designed solar cell was 17.19 mW/cm^2. When the bottom side length of the Al_2O_3 pyramid increased from 40 nm to 80 nm to 200 nm, the maximum electrical power showed a tendency to increase and then decrease. From Tables 1 and 2, it can be seen that when the Al_2O_3 PARLs had dimensions of h = 200 nm, d = 200 nm, the J_{SC} of the designed PSCs was 23.54 mA/cm^2 and the electrical power was 17.19 mW/cm^2; at this time, the photoelectric performance of the solar cells was at its best, and the anti-reflection effect of the Al_2O_3 structure was at its best.

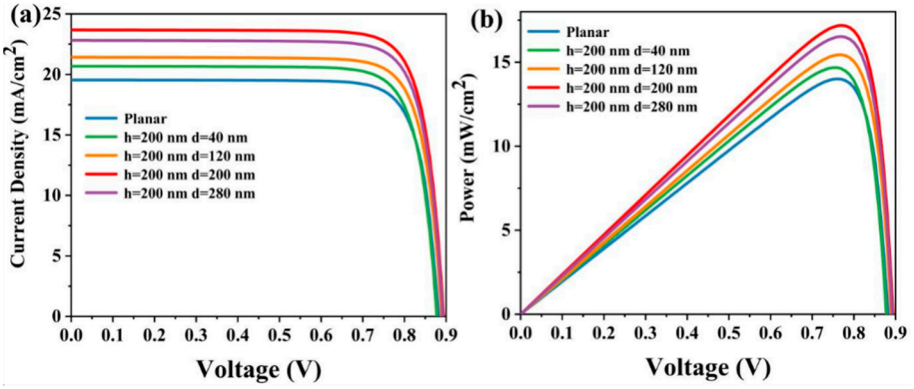


Figure 5. (**a**,**b**) J-V and P-V of the designed solar cells at different bottom side lengths of the Al_2O_3 pyramid, respectively.

Table 2. Specific parameters of the electrical performance of cells with different bottom edge lengths of Al_2O_3 pyramid.

d (nm)	V_{OC} (V)	J_{SC} (mA/cm^2)	PCE (%)
Planar	0.89	19.18	14.01
40	0.89	20.68	14.67
120	0.89	21.42	15.44
200	0.90	23.54	17.19
280	0.90	22.81	16.52

We know that the PSCs designed with the Al_2O_3 PARLs had the best photoelectric performance when the height h = 200 nm and the bottom side length d = 200 nm. Therefore, under the parameters of h = 200 nm and d = 200 nm, we compared the photoelectric characteristics of planar PSCs and Al_2O_3 pyramid PSCs. In FDTD, we calculated the reflection (R) and absorption (A) spectra of two differently structured cells, as shown in Figure 6a. These two structures are marked as the 'planar structure' and 'Al_2O_3 pyramid' in Figure 6a. The 'planar structure' represents a planar PSCs without Al_2O_3 PARLs, and the 'Al_2O_3 pyramid' represents a perovskite solar cell with an Al_2O_3 PARL structure. Figure 6a indicates that the PSCs with the Al_2O_3 PARLs significantly reduced the reflectivity within the wavelength range of 300 nm to 800 nm, which in turn enhanced absorption; the Al_2O_3 pyramid had an anti-reflection effect on the entire solar cell, and the overall light capture ability of the solar cell was greatly improved compared with the traditional 'planar structure' PSCs. It was observed that within the wavelength range of 300 nm to 800 nm, the light absorption rate of the Al_2O_3 pyramid was basically above 90%, while the light absorption of the planar structure was basically below 90%. This is because the Al_2O_3 pyramid structure on the surface of the solar cell was able to significantly reduce the reflectivity of the solar cell, enhance the light capture ability of the solar cell, and improve the light absorption of the solar cell [53,54]. In order to further compare the optical performance of the two structures of PSCs, we compared the light absorption efficiency of planar and Al_2O_3 pyramid PSCs under the AM 1.5 solar spectrum, as shown in Figure 6b. In Figure 6b, it can be seen that in the entire region of 300–800 nm, the average absorption rate of the Al_2O_3 pyramid structure reached 96.05%, while the average absorption rate of the planar structured cell was 87.41%, with the former increasing the average light absorption rate by 8.64%. The spectral absorption curve of the Al_2O_3 pyramid structure basically coincided with the solar energy spectrum at AM 1.5, indicating that the Al_2O_3 PARLs improved the light absorption of the PSCs in the visible light band [55].

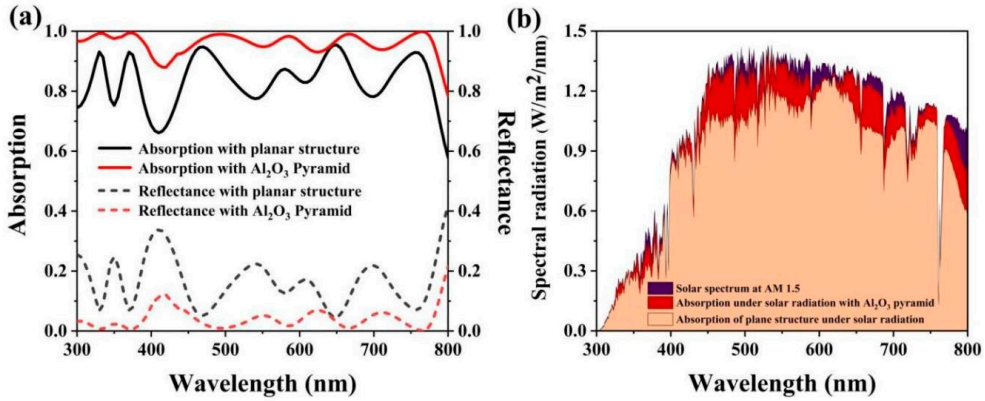


Figure 6. (**a**) The absorption and reflection spectra of the Al_2O_3 pyramid; (**b**) the comparison chart of the absorption spectra of planar and Al_2O_3 pyramid structures under the AM 1.5 solar spectrum.

QE is another important parameter to characterize the optical performance of PSCs. We also calculated the QE diagrams of the two structures and the corresponding integral currents. Figure 7a provides the QE curves and integral currents of the PSCs with Al_2O_3 pyramids in comparison with planar PSCs. It was observed that the two structures showed substantial differences in QE and integral current. The QE of the planar structure was much lower than that of the Al_2O_3 pyramid structure. The integral current value of the planar structure was also smaller than that of the Al_2O_3 pyramid structure. This result further verifies that the light capture ability of the structure with Al_2O_3 pyramids was greater than that of the planar structure [56,57]. In order to better compare the electrical characteristics of the two structures of PSCs, we used the finite element method to perform electrical simulation on the designed cells. As shown in the J-V curves in Figure 7b, the V_{OC} of the planar structure was 0.89 V, and its J_{SC} was 19.18 mA/cm^2. The short-circuit current of the J-V and the integral current of the QE were found to be in close proximity to one another and aligned with the QE results. The V_{OC} of the Al_2O_3 pyramid structure was 0.90 V, and its J_{SC} was 23.54 mA/cm^2. By establishing the surface Al_2O_3 PARLs, the J_{SC} of the solar cell was increased by 4.36 mA/cm^2. The above data prove that the Al_2O_3 pyramid PSCs had greatly improved short-circuit current density due to their significant anti-reflection benefits. In the P-V curve shown in Figure 7c, the Pmax of the planar structure PSCs is 14.01 mW/cm^2, and the Pmax of the Al_2O_3 pyramid structure is 17.19 mW/cm^2. Therefore, the PSCs with Al_2O_3 pyramids had a higher short-circuit current density and higher Pmax compared with the planar PSCs.

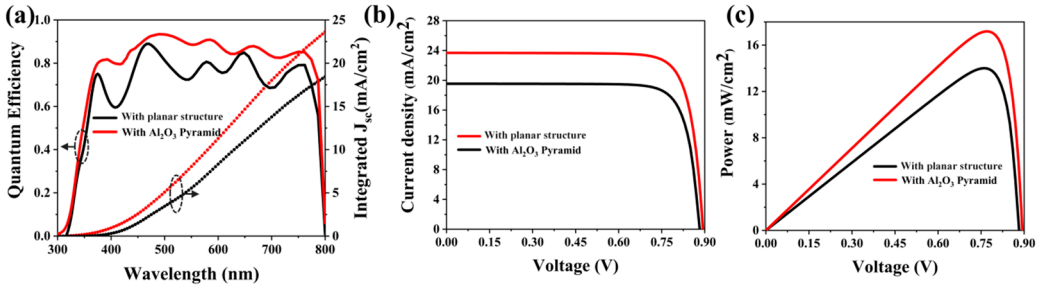


Figure 7. Diagrams of results for planar and Al_2O_3 pyramid structures: (**a**) QE curves and integral current; (**b**) J-V curves; (**c**) P-V curves.

Generally speaking, in order to better interpret the optical properties of a device, it is necessary to model its associated electromagnetic fields [58–60]. Here, in order to understand more clearly the propagation of incident light inside the solar cells before and after the assembly of the Al_2O_3 PARLs, Figure 8a–f illustrate the electric field intensity distribution of solar cells with and without Al_2O_3 PARLs at different wavelengths (λ = 300 nm, 410 nm, and 700 nm). Among them, Figure 8a–c represent the internal electric

field intensity distribution of the planar PSCs. Figure 8d–f show the internal electric field intensity distribution of the Al_2O_3 pyramid PSCs. Comparing the electric field intensity distribution between the two can indirectly explain the increase in the light absorption rate. For the electric field intensity distribution diagram, we chose the middle position in the *X*–*Z* plane. From Figure 8a–c, it can be seen that the planar PSCs induced the Fabry–Perot interference effect, responding to the electric field intensity as a striped pattern distributed along the *Z*-axis direction [61–63]. Compared with the planar PSCs, the Al_2O_3 PARLs enhanced the electric field intensity inside the perovskite light-absorbing layer, characterized by two bright local points at the edge of the model, as can be seen from Figure 8d–f. At λ = 300 nm, the electric field distribution of the planar PSCs was completely different from the electric field distribution of the perovskite solar cells with Al_2O_3 PARLs. Compared with the planar PSCs, the electric field intensity distribution on both sides and the inside of the top Al_2O_3 pyramid of the perovskite solar cells with Al_2O_3 PARLs was higher. There was no high electric field in the planar PSCs, and most of the spectral energy was distributed in the FTO/glass layer at this wavelength. In addition, compared with Figure 8b,e, under the Al_2O_3 pyramid structure, part of the spectral energy penetrated into the perovskite photosensitive layer. Comparing Figure 8c,f, in the Al_2O_3 pyramid PSCs in Figure 8f, except for the surroundings of the Al_2O_3 pyramid structure, the stripe width is almost the same as that in Figure 8c, but the electric field on both sides of the Al_2O_3 pyramid structure is significantly enhanced. This shows that the Al_2O_3 PARLs were able to excite guided-mode resonance in the perovskite absorption layer, corresponding to the periodic pattern of electric field intensity [64–66]. Therefore, due to the increase in the number of quasi-guided mode couplings, the electric field intensity was enhanced. The absorption of light is proportional to the electric field intensity, so the light absorption of the Al_2O_3 pyramid PSCs was higher, and the Al_2O_3 pyramid greatly improved the light absorption of the solar cells. In summary, the Al_2O_3 pyramid structure can adjust light coupling, has an anti-reflection effect, and has a good focusing effect on solar energy within the visible light range [67–69]. The existence of the Al_2O_3 pyramid structure enhances photon absorption, thereby generating more electron–hole pairs, so with the final increase in the photocurrent of solar cell, the overall performance of the solar cell is improved.

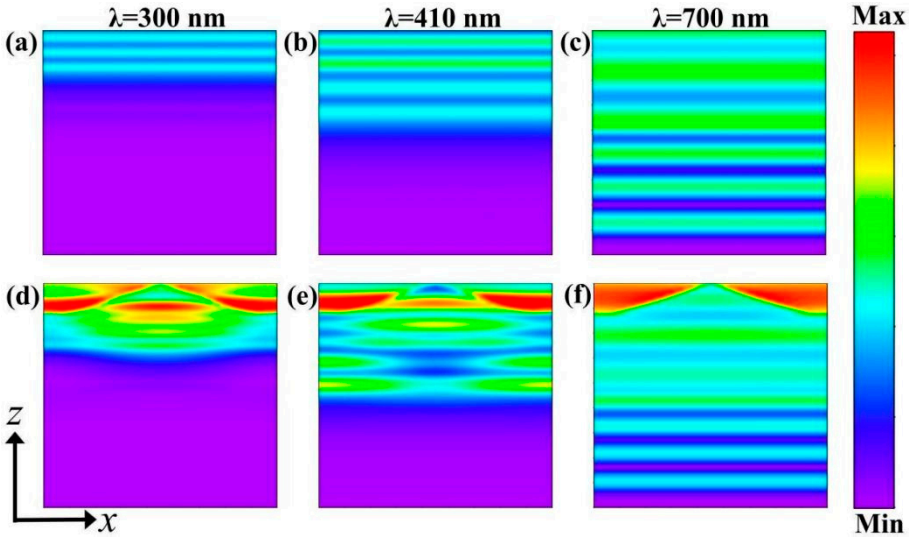


Figure 8. Field profiles of |E|, (**a**,**d**) planar PSCs and Al_2O_3 pyramid PSCs at 300 nm; (**b**,**e**) planar PSCs and Al_2O_3 pyramid PSCs at 410 nm; (**c**,**f**) planar PSCs and Al_2O_3 pyramid PSCs at 700 nm.

4. Conclusions

In this paper, we propose a perovskite solar cell based on an Al_2O_3 PARL structure, with a total thickness of 1400 nm. We analyzed the optoelectronic characteristics of Al_2O_3 pyramid PSCs in detail, and calculated the light absorption, QE, and various electrical

parameters of the solar cells by changing various parameters of the Al_2O_3 PARLs, including different heights and bottom lengths. Under the AM1.5 solar spectrum (300–800 nm), the average light absorption rate of the optimized Al_2O_3 pyramid was 96.05%, which was much higher than that of the planar structure. In addition, electrical simulation was carried out using the finite element method, and the J_{SC}, V_{OC}, and Pmax were calculated. Based on the maximum value of the average light absorbance, the geometric structure of the Al_2O_3 pyramid PSCs was optimized. The electrical simulation results showed that the maximum J_{SC} was 23.54 mA/cm^2 and the Jsc of the Al_2O_3 pyramid structure was 22.73% higher than that of the planar model, while the PCE of the solar cells increased from 14.01% to 17.19%. These results indicate that the ARL array had a strong light coupling effect, highlighting the great potential of Al_2O_3 PARLs for solar absorption. This work provides valuable insights for the structural design of PSCs and suggests that further exploration will lead to even greater improvements in the PCE of PSCs.

Author Contributions: Conceptualization, L.L., W.L., W.F., Z.Y. and C.T.; data curation, L.L., W.L., W.F., Z.Y., T.S., Q.Z. and P.W.; formal analysis, L.L., W.L., W.F., Z.Y., T.S., Q.Z. and P.W.; methodology, L.L., W.L., W.F., Z.Y. and T.S.; resources, Y.Y.; software, Y.Y., J.Z., C.T., T.S., T.S., Q.Z. and C.T.; data curation, L.L. and W.L.; writing—original draft preparation, L.L. and W.L.; writing—review and editing, L.L., W.L., W.F., Z.Y. and P.W. All authors have read and agreed to the published version of the manuscript.

Funding: The authors are grateful to the support from the National Natural Science Foundation of China (No. 51606158, 11604311, 12074151); the funding from the Natural Science Foundation of Fujian Province (2022J011102, 2022H0048); the funding from the Guangxi Science and Technology Base and Talent Special Project (No. AD21075009); the funding from the Sichuan Science and Technology Program (No. 2021JDRC0022); the funding from the Open Fund of the Key Laboratory for Metallurgical Equipment and Control Technology of the Ministry of Education in Wuhan University of Science and Technology, China (No. MECOF2022B01; MECOF2023B04); the funding from the project supported by Guangxi Key Laboratory of Precision Navigation Technology and Application, Guilin University of Electronic Technology (No. DH202321); the funding from the Doctoral Fund of Southwest University of Science and Technology (no. 21zx7111); the funding from the Postgraduate Innovation Fund Project of Southwest University of Science and Technology (No. 24ycx1007).

Institutional Review Board Statement: Not applicable.

Informed Consent Statement: Not applicable.

Data Availability Statement: Publicly available datasets were analyzed in this study. This data can be found here: https://www.lumerical.com/.

Conflicts of Interest: The authors declare no conflicts of interest.

References

1. Park, N.G. Perovskite solar cells: An emerging photovoltaic technology. *Mater. Today* **2015**, *18*, 65–72. [CrossRef]
2. Serpetzoglou, E.; Konidakis, I.; Kourmoulakis, G.; Demeridou, I.; Chatzimanolis, K.; Zervos, C.; Kioseoglou, G.; Kymakis, E.; Stratakis, E. Charge carrier dynamics in different crystal phases of $CH_3NH_3PbI_3$ perovskite. *Opto-Electron. Sci.* **2022**, *1*, 210005. [CrossRef]
3. Heo, J.H.; You, M.S.; Chang, M.H.; Yin, W.; Ahn, T.K.; Lee, S.J.; Sung, S.J.; Kim, D.H.; Im, S.H. Hysteresis-less mesoscopic $CH_3NH_3PbI_3$ perovskite hybrid solar cells by introduction of Li-treated TiO_2 electrode. *Nano Energy* **2015**, *15*, 530–539. [CrossRef]
4. Shen, T.Y.; Qin, J.J.; Bai, Y.J.; Zhang, J.; Shi, L.; Hou, X.; Zi, J.; Hu, B. Giant magneto field effect in up-conversion amplified spontaneous emission via spatially extended states in organic-inorganic hybrid perovskites. *Opto-Electron. Adv.* **2022**, *5*, 200051. [CrossRef]
5. Han, Q.C.; Liu, S.W.; Liu, Y.Y.; Jin, J.S.; Li, D.; Cheng, S.B.; Xiong, Y. Flexible counter electrodes with a composite carbon/metal nanowire/polymer structure for use in dye-sensitized solar cells. *Sol. Energy* **2020**, *208*, 469–479. [CrossRef]
6. Lu, T.W.; Lin, Y.; Zhang, T.Q.; Huang, Y.; Fan, X.; Lai, S.; Lu, Y.; Kuo, H.-C.; Chen, Z.; Wu, T.; et al. Self-polarized RGB device realized by semipolar micro-LEDs and perovskite-in-polymer films for backlight applications. *Opto-Electron. Adv.* **2024**, *7*, 230210. [CrossRef]
7. Maleki, J.; Eskandari, M.; Fathi, D. PbS-TBAI/$MoSe_2$-grating as new hole transport layer in perovskite solar cells: Superior efficiency enhancement thru simulation and optimization. *J. Alloys Compd.* **2023**, *960*, 170653. [CrossRef]

8. Zhang, Y.; Yi, Y.; Li, W.; Liang, S.; Ma, J.; Cheng, S.; Yang, W.; Yi, Y. High Absorptivity and Ultra-Wideband So-lar Absorber Based on Ti-Al_2O_3 Cross Elliptical Disk Arrays. *Coatings* **2023**, *13*, 531. [CrossRef]
9. Mortadi, A.; El Hafidi, E.; Monkade, M.; El Moznine, R. Investigating the influence of absorber layer thickness on the performance of perovskite solar cells: A combined simulation and impedance spectroscopy study. *Mater. Sci. Energy Technol.* **2024**, *7*, 158–165. [CrossRef]
10. Zheng, Y.; Wang, Z.Y.; Yi, Z.; Cheng, S.B.; Ma, C.; Tang, B.; Sun, T.Y.; Yu, S.J.; Li, G.F.; Ahmad, S. A wide-band solar absorber based on tungsten nano-strip resonator group and graphene for near-ultraviolet to near-infrared re-gion. *Diam. Relat. Mater.* **2024**, *142*, 110843. [CrossRef]
11. Elbanna, A.; Chaykun, K.; Lekina, Y.; Liu, Y.D.; Febriansyah, B.; Li, S.; Pan, J.; Shen, Z.X.; Teng, J. Perovskite-transition metal dichalcogenides heterostructures: Recent advances and future perspectives. *Opto-Electron. Sci.* **2022**, *1*, 220006. [CrossRef]
12. Waddell, E.; Gibson, D.; Lin, L.; Fu, X. Modelling and optimization of film thickness variation for plasma enhanced chemical vapour deposition processes. *Proc. SPIE-Int. Soc. Opt. Eng.* **2013**, *8168*, 259–264. [CrossRef]
13. Thomas, S.; Nalini, S.; Kumar, K.R. Microwave plasma-assisted ALD of Al_2O_3 thin films: A study on the substrate temperature dependence of various parameters of interest. *Appl. Phys. A* **2017**, *123*, 185. [CrossRef]
14. Aliyariyan, M.; Fathi, D.; Eskandari, M.; Tooghi, A. Efficiency enhancement of perovskite solar cells by designing GeSe nanowires in the structure of adsorbent layer. *Nanotechnology* **2020**, *31*, 465405. [CrossRef] [PubMed]
15. Mohammadi, M.H.; Fathi, D.; Eskandari, M. NiO@GeSe core-shell nano-rod array as a new hole transfer layer in perovskite solar cells: A numerical study. *Sol. Energy* **2020**, *204*, 200–207. [CrossRef]
16. Mohammadi, M.H.; Fathi, D.; Eskandari, M. Light trapping in perovskite solar cells with plasmonic core/shell nanorod array: A numerical study. *Energy Rep.* **2021**, *7*, 1404–1415. [CrossRef]
17. Aliyariyan, M.; Fathi, D.; Eskandari, M.; Mohammadi, M.H. Simulation and investigation of perovskite/nano-pyramidal GeSe solar cell: Realizing high efficiency by controllable light trapping. *Sol. Energy* **2021**, *214*, 310–318. [CrossRef]
18. Chen, J.Y.; Yu, M.H.; Chang, S.F.; Sun, K.W. Highly efficient poly (3,4-ethylenedioxythiophene): Poly (styrenesulfonate)/Si hybrid solar cells with imprinted nanopyramid structures. *Appl. Phys. Lett.* **2013**, *103*, 133901. [CrossRef]
19. Xiao, T.X.; Tu, S.; Liang, S.Z.; Guo, R.J.; Tian, T.; Müller-Buschbaum, P. Solar cell-based hybrid energy harvesters towards sustainability. *Opto-Electron. Sci.* **2023**, *2*, 230011. [CrossRef]
20. Leem, J.W.; Kim, S.; Lee, S.H.; Rogers, J.A.; Kim, E.; Yu, J.S. Efficiency Enhancement of Organic Solar Cells Using Hydrophobic Antireflective Inverted Moth-Eye Nanopatterned PDMS Films. *Adv. Energy Mater.* **2014**, *4*, 1301315. [CrossRef]
21. Park, C.H.; Kim, J.Y.; Sung, S.-J.; Kim, D.-H.; Do, Y.S. Design of Grating Al_2O_3 Passivation Structure Optimized for High-Efficiency Cu(In,Ga)Se_2 Solar Cells. *Sensors* **2021**, *21*, 4849. [CrossRef] [PubMed]
22. Liang, S.R.; Xu, F.; Li, W.X.; Yang, W.X.; Cheng, S.B.; Yang, H.; Chen, J.; Yi, Z.; Jiang, P.P. Tunable smart mid infrared thermal control emitter based on phase change material VO_2 thin film. *Appl. Therm. Eng.* **2023**, *232*, 121074. [CrossRef]
23. Fan, W.; Shen, H.; Liu, B.; Zhao, L.; Zhang, X.; Pan, H. Influence of Al_2O_3/SiN_x Rear-Side Stacked Passivation on the Performance of Polycrystalline PERC Solar Cells. *Energies* **2023**, *16*, 6963. [CrossRef]
24. Gu, Y.; Chen, S.; Lin, J.; Xu, H.; Li, X. High-quality efficient anti-reflection nanopillar structures layer prepared by a new type vibration-assisted UV nanoimprint lithography. *J. Manuf. Process.* **2021**, *61*, 461–472. [CrossRef]
25. Park, J.; Kim, J.; Yun, H.S.; Paik, M.J.; Noh, E.; Mun, H.J.; Kim, M.G.; Shin, T.J.; Seok, S.I. Controlled growth of perovskite layers with volatile alkylammonium chlorides. *Nature* **2023**, *616*, 724–730. [CrossRef] [PubMed]
26. Liang, S.; Cheng, S.; Zhang, H.; Yang, W.; Yi, Z.; Zeng, Q.; Tang, B.; Wu, P.; Ahmad, S.; Sun, T. Structural color tunable intelligent mid-infrared thermal control emitter. *Ceram. Int.* **2024**, *50*, 23611–23620. [CrossRef]
27. Cheng, S.; Li, W.; Zhang, H.; Akhtar, M.N.; Yi, Z.; Zeng, Q.; Ma, C.; Sun, T.; Wu, P.; Ahmad, S. High sensitivity five band tunable metamaterial absorption device based on block like Dirac semimetals. *Opt. Commun.* **2024**, *569*, 130816. [CrossRef]
28. Ma, J.; Wu, P.H.; Li, W.X.; Liang, S.R.; Shangguan, Q.Y.; Cheng, S.B.; Tian, Y.H.; Fu, J.Q.; Zhang, L.B. A five-peaks graphene ab-sorber with multiple adjustable and high sensitivity in the far infrared band. *Diam. Relat. Mater.* **2023**, *136*, 109960. [CrossRef]
29. Maksimovic, J.; Hu, J.W.; Ng, S.H.; Katkus, T.; Seniutinas, G.; Rivera, T.P.; Stuiber, M.; Nishijima, Y.; John, S.; Juodkazis, S.; et al. Beyond Lambertian light trapping for large-area silicon solar cells: Fabrication methods. *Opto-Electron. Adv.* **2022**, *5*, 210086. [CrossRef]
30. Xiong, H.; Deng, J.H.; Yang, Q.; Wang, X.; Zhang, H. A metamaterial energy power detector based on electro-magnetic energy harvesting technology. *ACS Appl. Electron. Mater.* **2024**, *6*, 1204–1210. [CrossRef]
31. Li, W.X.; Zhao, W.C.; Cheng, S.B.; Zhang, H.F.; Yi, Z.; Sun, T.Y.; Wu, P.H.; Zeng, Q.D.; Raza, R. Tunable Metamaterial Absorption Device based on Fabry–Perot Resonance as Temperature and Refractive Index Sensing. *Opt. Lasers Eng.* **2024**, *181*, 108368. [CrossRef]
32. Gigli, C.; Leo, G. All-dielectric χ(2) metasurfaces: Recent progress. *Opto-Electron. Adv.* **2022**, *5*, 210093. [CrossRef]
33. Chen, Z.Y.; Cheng, S.B.; Zhang, H.F.; Yi, Z.; Tang, B.; Chen, J.; Zhang, J.G.; Tang, C.J. Ultra wideband absorption absorber based on Dirac semimetallic and graphene metamaterials. *Phys. Lett. A* **2024**, *517*, 129675. [CrossRef]
34. Xiong, H.; Ma, X.D.; Wang, B.X.; Zhang, H.Q. Design and analysis of an electromagnetic energy conversion device. *Sens. Actuators A Phys.* **2024**, *366*, 114972. [CrossRef]
35. Luo, J.; Zhang, J.H.; Gao, S.S. Design of Multi-Band Bandstop Filters Based on Mixed Electric and Magnetic Coupling Resonators. *Electronics* **2024**, *13*, 1552. [CrossRef]

36. Li, W.; Cheng, S.; Zhang, H.; Yi, Z.; Tang, B.; Ma, C.; Wu, P.; Zeng, Q.; Raza, R. Multi-functional metasurface: Ul-tra-wideband/multi-band absorption switching by adjusting guided mode resonance and local surface plasmon resonance effects. *Commun. Theor. Phys.* **2024**, *76*, 065701. [CrossRef]
37. Li, W.X.; Liu, Y.H.; Ling, L.; Sheng, Z.X.; Cheng, S.B.; Yi, Z.; Wu, P.H.; Zeng, Q.D.; Tang, B.; Ahmad, S. The tunable absorber films of grating structure of AlCuFe quasicrystal with high Q and refractive index sensitivity. *Surf. Inter-Faces* **2024**, *48*, 104248. [CrossRef]
38. Deng, X.; Shui, T.; Yang, W.X. Inelastic two-wave mixing induced high-efficiency transfer of optical vortices. *Opt. Express* **2024**, *32*, 16611–16628. [CrossRef] [PubMed]
39. Liang, X.; Guan, H.; Luo, K.; He, Z.; Liang, A.; Zhang, W.; Lin, Q.; Yang, Z.; Zhang, H.; Xu, C.; et al. Van der Waals integrated $LiNbO_3/WS_2$ for High-Performance UV-Vis-NIR Photodetection. *Laser Photonics Rev.* **2023**, *17*, 2300286. [CrossRef]
40. Li, W.X.; Liu, M.S.; Cheng, S.B.; Zhang, H.F.; Yang, W.X.; Yi, Z.; Zeng, Q.D.; Tang, B.; Ahmad, S.; Sun, T.Y. Po-lar-ization inde-pendent tunable bandwidth absorber based on single-layer graphene. *Diam. Relat. Mater.* **2024**, *142*, 110793. [CrossRef]
41. Xie, Y.; Liu, Z.; Zhou, F.; Luo, X.; Gong, Y.; Cheng, Z.; You, Y. Tunable nonreciprocal metasurfaces based on nonlinear quasi-Bound state in the Continuum. *Opt. Lett.* **2024**, *49*, 3520–3523. [CrossRef] [PubMed]
42. Zhu, J.; Xiong, J.Y. Logic operation and all-optical switch characteristics of graphene surface plasmons. *Opt. Express* **2023**, *31*, 36677. [CrossRef] [PubMed]
43. Li, W.X.; Xu, F.; Cheng, S.B.; Yang, W.X.; Liu, B.; Liu, M.S.; Yi, Z.; Tang, B.; Chen, J.; Sun, T.Y. Six-band rotation-ally symmetric tunable absorption film based on AlCuFe quasicrystals. *Opt. Laser Technol.* **2024**, *169*, 110186. [CrossRef]
44. Kumar, P.; Huang, S.-H.; Hsu, C.-Y.; Chung, S.-Y.; Cha, H.-C.; Chuang, C.-M.; Chen, K.-L.; Huang, Y.-C. Enhancing Power Conversion Efficiency of Organic Solar Cells with Magnetoplasmonic Fe_3O_4@Au@m-ABS Nanoparticles. *Nanomaterials* **2024**, *14*, 1175. [CrossRef]
45. Luo, J. Dynamical behavior analysis and soliton solutions of the generalized Whitham–Broer–Kaup–Boussineq–Kupershmidt equations. *Results Phys.* **2024**, *60*, 107667. [CrossRef]
46. He, Z.; Guan, H.; Liang, X.; Chen, J.; Xie, M.; Luo, K.; An, R.; Ma, L.; Ma, F.; Yang, T.; et al. Broadband, polarization-sensitive, and self-powered high-performance photodetection of hetero-integrated MoS_2 on lithium niobate. *Research* **2023**, *6*, 0199. [CrossRef] [PubMed]
47. David, C.; Koduvelikulathu, L.J.; Kopecek, R. Comparative Simulations of Conductive Nitrides as Alternative Plasmonic Nanostructures for Solar Cells. *Energies* **2021**, *14*, 4236. [CrossRef]
48. Shangguan, Q.; Zhao, Y.; Song, Z.; Wang, J.; Yang, H.; Chen, J.; Liu, C.; Cheng, S.; Yang, W.; Yi, Z. High sensitivi-ty active adjustable graphene absorber for refractive index sensing applications. *Diam. Relat. Mater.* **2022**, *128*, 109273. [CrossRef]
49. Li, W.; Ma, J.; Zhang, H.; Cheng, S.; Yang, W.; Yi, Z.; Yang, H.; Zhang, J.; Wu, X.; Wu, P. Tunable broadband ab-sorber based on a layered resonant structure with a Dirac semimetal. *Phys. Chem. Chem. Phys.* **2023**, *25*, 8489–8496. [CrossRef] [PubMed]
50. Lei, W.; He, Q.; Yang, L.; Jiao, H. Solar Photovoltaic Cell Parameter Identification Based on Improved Honey Badger Algorithm. *Sustainability* **2022**, *14*, 8897. [CrossRef]
51. Deng, J.H.; Xiong, H.; Yang, Q.; Wang, B.X.; Zhang, H.Q. Metasurface-based Microwave Power Detector for Polarization Angle Detection. *IEEE Sens. J.* **2023**, *23*, 22459–22465. [CrossRef]
52. Li, W.X.; Zhao, W.C.; Cheng, S.B.; Yang, W.X.; Yi, Z.; Li, G.F.; Zeng, L.C.; Li, H.L.; Wu, P.H.; Cai, S.S. Terahertz Selec-tive Active Electromagnetic Absorption Film Based on Single-layer Graphene. *Surf. Interfaces* **2023**, *40*, 103042. [CrossRef]
53. Zhang, T.X.; Tao, C.; Ge, S.X.; Pan, D.W.; Li, B.; Huang, W.X.; Wang, W.; Chu, L.Y. Interfaces coupling defor-mation mechanisms of liquid-liquid-liquid three-phase flow in a confined microchannel. *Chem. Eng.-Ing. J.* **2022**, *434*, 134769. [CrossRef]
54. Alamri, Y.A.; Mahmoud, S.; Al-Dadah, R.; Sharma, S.; Roy, J.N.; Ding, Y. Optical Performance of Single Point-Focus Fresnel Lens Concentrator System for Multiple Multi-Junction Solar Cells—A Numerical Study. *Energies* **2021**, *14*, 4301. [CrossRef]
55. Liang, S.; Xu, F.; Yang, H.; Cheng, S.; Yang, W.; Yi, Z.; Song, Q.; Wu, P.; Chen, J.; Tang, C. Ultra long infrared met-amaterial absorber with high absorption and broad band based on nano cross surrounding. *Opt. Laser Technol.* **2023**, *158*, 108789. [CrossRef]
56. Li, W.; Yi, Y.; Yang, H.; Cheng, S.; Yang, W.X.; Zhang, H.; Yi, Z.; Yi, Y.; Li, H. Active Tunable Terahertz Band-width Absorber Based on single layer Graphene. *Commun. Theor. Phys.* **2023**, *75*, 045503. [CrossRef]
57. Ma, Z.; Li, R.; Xiong, R.; Zhang, Y.; Xu, C.; Wen, C.; Sa, B. InSe/Te van der Waals Heterostructure as a High-Efficiency Solar Cell from Computational Screening. *Materials* **2021**, *14*, 3768. [CrossRef] [PubMed]
58. Shangguan, Q.; Chen, H.; Yang, H.; Liang, S.; Zhang, Y.; Cheng, S.; Yang, W.; Yi, Z.; Luo, Y.; Wu, P. A "bel-fry-typed" narrow-band tunable perfect absorber based on graphene and the application potential research. *Diam. Relat. Mater.* **2022**, *125*, 108973. [CrossRef]
59. Shui, T.; Chen, X.M.; Yang, W.X. Coherent control of spatial and angular Goos-Hänchen shifts with spontaneously generated co-herence and incoherent pumping. *Appl. Opt.* **2022**, *61*, 10072–10079. [CrossRef] [PubMed]
60. Shangguan, Q.; Chen, Z.; Yang, H.; Cheng, S.; Yang, W.; Yi, Z.; Wu, X.; Wang, S.; Yi, Y.; Wu, P. Design of Ul-tra-Narrow Band Graphene Refractive Index Sensor. *Sensors* **2022**, *22*, 6483. [CrossRef] [PubMed]
61. Wu, F.Y.; Liu, Y.H.; Ling, L.; Sheng, Z.X.; Yi, Z.; Song, Q.J.; Cheng, S.B.; Tang, B.; Ahmad, S.; Sun, T.Y. Spectrally Selective Ultra-Broadband Solar Absorber Based on Pyramidal Structure. *Adv. Photonics Res.* **2024**, *5*, 2300305. [CrossRef]
62. Zhu, J.; Xiong, J.Y. Tunable terahertz graphene metamaterial optical switches and sensors based on plasma-induced transparency. *Measurement* **2023**, *220*, 113302. [CrossRef]

63. Fu, R.; Chen, K.X.; Li, Z.L.; Yu, S.H.; Zheng, G.X. Metasurface-based nanoprinting: Principle, design and advances. *Opto-Electron. Sci.* **2022**, *1*, 220011. [CrossRef]
64. Zheng, Y.; Zhao, W.; Song, Q.; Ma, C.; Yi, Z.; Zeng, Q.; Sun, T.; Chen, J.; Yan, J. Analysis of solar absorption and thermal radiation properties of a multi-layer structure. *Int. J. Therm. Sci.* **2024**, *203*, 109172. [CrossRef]
65. Gao, H.; Fan, X.; Wang, Y.; Liu, Y.; Wang, X.; Xu, K.; Deng, L.; Zeng, C.; Li, T.; Xia, J.; et al. Multi-foci metalens for spectra and polarization ellipti-city recognition and reconstruction. *Opto-Electron. Sci.* **2023**, *2*, 220026. [CrossRef]
66. Xiong, H.; Ma, X.D.; Liu, H.S.; Xiao, D.P.; Zhang, H.Q. Research on Electromagnetic Energy Absorption and Conversion Device with Four-Ring Multi-Resistance Structure. *Appl. Phys. Lett.* **2023**, *123*, 153902. [CrossRef]
67. Sang, T.; Mi, Q.; Yang, C.Y.; Zhang, X.H.; Wang, Y.K.; Ren, Y.Z.; Xu, T. Achieving asymmetry parameter-insensitive resonant modes through relative shift–induced quasi-bound states in the continuum. *Nanophotonics* **2024**, *13*, 1369–1377. [CrossRef]
68. Baeva, M.; Gets, D.; Polushkin, A.; Vorobyov, A.; Goltaev, A.; Neplokh, V.; Mozharov, A.; Krasnikov, D.V.; Nasibulin, A.G.; Mukhin, I.; et al. ITO-free silicon-integrated perovskite electrochemical cell for light-emission and light-detection. *Opto-Electron. Adv.* **2023**, *6*, 220154. [CrossRef]
69. Lee, S.M.; Kwong, A.; Jung, D.; Faucher, J.; Biswas, R.; Shen, L.; Kang, D.; Lee, M.L.; Yoon, J. High Performance Ultrathin GaAs Solar Cells Enabled with Heterogeneously Integrated Dielectric Periodic Nanostructures. *ACS Nano* **2015**, *9*, 10356–10365. [CrossRef] [PubMed]

Disclaimer/Publisher's Note: The statements, opinions and data contained in all publications are solely those of the individual author(s) and contributor(s) and not of MDPI and/or the editor(s). MDPI and/or the editor(s) disclaim responsibility for any injury to people or property resulting from any ideas, methods, instructions or products referred to in the content.